Merger and Mass Ejection of Neutron-Star Binaries

Masaru Shibata,[1] and Kenta Hotokezaka[2]

[1]Max Planck Institute for Gravitational Physics (Albert Einstein Institute), Am Mühlenberg 1, PotsdamG-olm, D-14476, German, and Center for Gravitational Physics, Yukawa Institute for Theoretical Physics, Kyoto University, Kyoto 606-8502, Japan
[2]Department of Astrophysical Sciences, Princeton University, Princeton, NJ 08544, USA

Abstract

Mergers of binary neutron stars and black hole-neutron star binaries are one of the most promising sources for the ground-based gravitational-wave (GW) detectors and also a high-energy astrophysical phenomenon as illustrated by the observations of gravitational waves and electromagnetic (EM) waves in the event of GW170817. Mergers of these neutron-star binaries are also the most promising site for r-process nucleosynthesis. Numerical simulation in full general relativity (numerical relativity) is a unique approach to the theoretical prediction of the merger process, GWs emitted, mass ejection process, and resulting EM emission. We summarize our current understanding for the processes of neutron star mergers and subsequent mass ejection based on the results of the latest numerical-relativity simulations. We emphasize that the predictions of the numerical-relativity simulations agrees broadly with the optical and infrared observations of GW170817.

Contents

1. INTRODUCTION

Mergers of neutron-star binaries [binary neutron stars and black hole-neutron star (BH-NS) binaries] are one of the most promising sources of gravitational waves (GWs) for ground-based detectors, such as Advanced LIGO, Advanced Virgo, and KAGRA (1, 2, 3). Advanced LIGO and Advanced Virgo made the first observation of GWs from a binary neutron star on August 17, 2017 (GW170817) (4). We expect that these GW observatories will detect a number of signals from neutron star binaries in the next few years.

Neutron star mergers are also attracting attention as promising nucleosynthesis sites of heavy elements through the rapid neutron capture process (r-process) (5, 6, 7), because a significant amount of neutron-rich matter is likely to be ejected during merger (see Refs. (8, 9, 10, 11) for the pioneering research). In association with the production of neutron-rich heavy elements in the merger ejecta, a strong electromagnetic (EM) emission (kilonova/macronova) is predicted to be powered by the subsequent radioactive decay of the r-process elements (12, 13, 14, 15, 16, 17, 18). This will be an EM counterpart of GWs from neutron star mergers and its detection could be used to verify the neutron star merger scenario for the origin of r-process elements. This hypothesis is strengthen by the observation of ultra-violet, optical, and infrared signals of GW170817 (19, 20, 21, 22, 23, 24, 25, 26, 27, 28, 29). In addition to kilonovae, a long-lasting synchrotron emission in multi-wavelengths could arise from the interaction of the merger ejecta with the interstellar medium (ISM) (30). To detect such signals is a unique probe to study the velocity profile of the merger ejecta. All these facts have encouraged the community of GW astronomy to theoretically explore the mass ejection mechanisms, r-process nucleosynthesis, and associated EM emission in neutron star mergers.

To study these topics quantitatively, we must clarify the merger process, subsequent mass ejection, nucleosynthesis and subsequent decay of heavy elements in the ejecta, and EM emission arising from the ejecta. Numerical-relativity simulations that take into account the detailed microphysical processes, neutrino radiation transfer, and magnetohydrodynamics

(MHD), are currently our best approach to the problem. Considerable efforts have been devoted to developing numerical-relativity simulations for neutron star mergers over the past two decades, since the first successful simulation of a binary neutron star merger in 1999 (31, 32). Now, detailed modeling for the merger phenomena is feasible. In particular, during the last decade, researchers have performed a wide variety of numerical-relativity simulations, taking into account finite-temperature effects for neutron star equations of state (EOSs) (33, 34), neutrino cooling (34, 35, 36, 37) and neutrino heating (38, 39), and MHD instability (40, 41, 42), have been performed. Numerical relativity has become a robust tool to study merger phenomena, and it allows us to predict observational features of neutron star mergers.

The mass ejection processes have been explored with numerical-relativity simulations since the publications by Hotokezaka et al. (43) for binary neutron stars and by Foucart et al. (44) for BH-NS binaries (see also Bauswein et al. (45) for an approximately general-relativistic work). A variety of numerical-relativity simulations have been performed to explore the nature of dynamical ejecta (38, 37, 46, 47, 48, 49, 39, 50, 51, 52, 53, 54, 55, 56, 57, 58). These publications have clarified that the mass of the dynamically ejected matter during merger depends strongly on the EOS, total mass and mass ratio of the system, and BH spin (for BH-NS binaries). For binary neutron stars, the ejecta components have a somewhat broad range of electron fraction between ≈ 0.05 and ≈ 0.5 irrespective of the EOS, where the electron fraction denoted by Y_e is the electron number density per baryon number density. This broad Y_e distribution is well suited for explaining the abundance patterns of r-process elements with mass numbers larger than $A \sim 90$ observed in the Solar System and metal-poor stars (59, 52). By contrast, for BH-NS binaries, the electron fraction of the dynamical ejecta is always low ($Y_e \lesssim 0.1$), and hence, heavy r-process elements ($A \gtrsim 130$) are dominantly synthesized (60).

After a binary neutron star merger, a BH or massive neutron star (MNS) surrounded by a dense massive disk (or torus) is formed. Since 2013, various simulations for the evolution of such post-merger remnants have been performed (61, 62, 63, 64, 65, 60, 66, 67, 68). These simulations have indicated that a large fraction of mass of compact disks surrounding the central compact objects is ejected from the system by a viscous, nuclear recombination, and/or MHD effect. The mass of this ejecta can be of order $10^{-2}M_\odot$; thus, it can dominate over the mass of dynamical ejecta, implying that this ejecta is as important as or even more important than dynamical ejecta to power EM emission.

The purpose of this article is to review the merger process and mass ejection mechanisms in neutron star merger, and to summarize possible EM emission from the merger ejecta. This review is organized as follows. In § 2, we summarize processes of the merger and post-merger phases of neutron star binaries based on the latest results of numerical-relativity simulations. In § 3, we describe mass ejection processes during merger and from the post-merger remnants. In § 4, we list the representative EM signals (ultra-violet, optical, infrared, and radio signals) emitted from the ejecta of neutron-star mergers. Finally, in § 5, we note that the optical and infrared signals of GW170817 are consistent broadly with the prediction by numerical relativity.

2. SCENARIOS FOR NEUTRON-STAR MERGER AND POST MERGER

The fate of neutron star mergers depends on the mass (m_1, m_2) and spin of binary components, and on the neutron star EOS. For binary neutron stars, for which the effect of

prompt BH formation ← $m > M_{\mathrm{thr}}$ $m < M_{\mathrm{thr}}$ → MNS formation

Merger

$m < M_{\mathrm{max,spin}}$

HMNS   SMNS

$m_1 \approx m_2$ $m_1 \neq m_2$

hydrodynamics / viscous evolution

BH+tine disk   BH+disk   BH+disk   SMNS+disk

viscous evolution of disk
disk matter infall/outflow

Isolated BH   spin down   cool down
collapse

Higher total mass, m
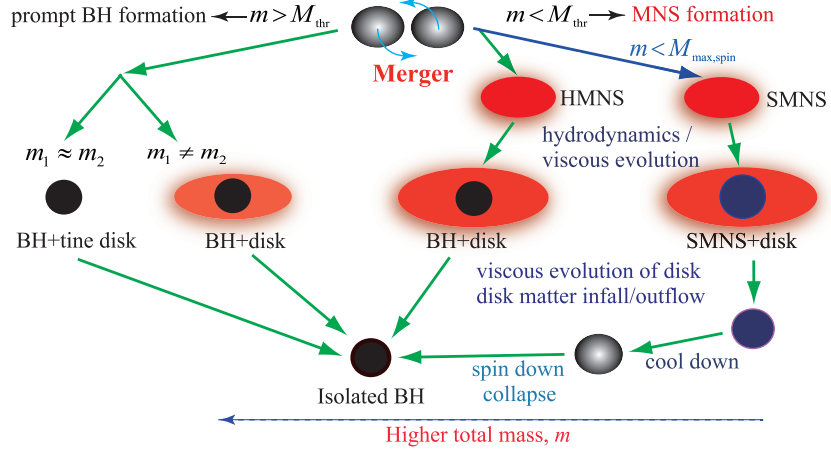
Figure 1

A summary for the merger and post-merger evolution of binary neutron stars. M_{thr} and $M_{\mathrm{max,spin}}$ denote the threshold mass for the prompt formation of a BH and the maximum mass of rigidly rotating cold neutron stars, respectively. Their values are likely to be $M_{\mathrm{thr}} \gtrsim 2.8 M_\odot$ and $M_{\mathrm{max,spin}} \gtrsim 2.4 M_\odot$. For the total mass $m > M_{\mathrm{thr}}$, a BH is formed in the dynamical timescale after the onset of merger, and for the nearly equal-mass case, $m_1 \approx m_2$, the mass of disks surrounding the BH is tiny $\ll 10^{-2} M_\odot$, while it could be $\gtrsim 10^{-2} M_\odot$ for a highly asymmetric system with $m_2/m_1 \lesssim 0.8$. For $M_{\mathrm{max,spin}} < m < M_{\mathrm{thr}}$, a *hypermassive* neutron star (HMNS) is formed, and it subsequently evolves through several angular-momentum transport processes, leading to eventual collapse to a BH surrounded by a disk (or torus). See Refs. (69, 70) for the definition of the HMNS (and SMNS referred to below). When m is close to M_{thr}, the lifetime of the MNS is relatively short, while for smaller values of m toward $M_{\mathrm{max,spin}}$, the lifetime is longer. For the longer lifetime, the angular-momentum transport process works for a longer timescale, and the disk mass could be $\gtrsim 0.1 M_\odot$, whereas for a short lifetime, it could be $\sim 10^{-2} M_\odot$ or less. For $m < M_{\mathrm{max,spin}}$, a *supramassive* neutron star (SMNS) is formed and it will be alive for a dissipation timescale of angular momentum which will be much longer than the cooling timescale $\sim 10\,\mathrm{s}$. Note that MNS denotes either a SMNS or a HMNS.

their spin is minor, the total mass ($m = m_1 + m_2$), the mass ratio ($q = m_2/m_1\ (\leq 1)$) of the system, and the EOS are the key quantities for determining the merger remnant. For BH-NS binaries, the BH spin as well as the mass ratio and neutron-star EOS are the key quantities. In the following two subsections, we classify the remnants formed after neutron-star mergers.

2.1. Binary Neutron Stars

Figure 1 summarizes the possible remnants and their evolution processes for mergers of binary neutron stars. Broadly speaking, there are two possible remnants formed immediately after the onset of merger; BH and MNS. A BH is formed if the total mass m is so high that the self gravity of the merger remnant cannot be sustained by the pressure associated primarily with the repulsive force among nucleons and centrifugal force due to rapid rotation associated with the orbital angular momentum of the premerger binary.

In the last decade, simulations were performed employing a variety of neutron-star EOSs (e.g., (73, 74, 75, 76, 43, 77, 78, 79, 80, 38, 37, 52, 49, 39, 81)), of which the maximum mass of a non-rotating neutron star is consistent with the existence of two-solar-mass neutron

stars (71, 72). An important finding for these simulations is that for $m \lesssim 2.8 M_\odot$, the remnant is, at least temporarily, an MNS not a BH irrespective of the EOS employed.

The total mass of nine Galactic binary neutron stars for which the merger time is less than a Hubble time of $\sim 13.8\,\mathrm{Gyr}$ is in the range between $\approx 2.50 M_\odot$ and $2.88 M_\odot$ (82, 83). Among them, seven objects have a total mass smaller than $2.75 M_\odot$, suggesting that, for the typical total mass of binary neutron stars, an MNS should be formed after merger (at least temporarily). In fact, the total mass of the binary neutron star GW170817 is in the middle of the above range, $2.74^{+0.04}_{-0.01} M_\odot$, for a low spin prior (4).

For $m \gtrsim 2.8 M_\odot$, a BH could be formed immediately after merger, although the threshold mass for the prompt BH formation depends strongly on the EOS. The dimensionless BH spin, χ, in the prompt BH formation case is ≈ 0.8 (75). The remnant BH in this formation channel is not surrounded by a massive disk if the mass ratio, q, is close to unity. The mass of the disk surrounding the BH increases with the decrease of q, and in the presence of a significant mass asymmetry, $q \lesssim 0.8$, the disk mass could be $\gtrsim 10^{-2} M_\odot$ (74, 75, 77). The disk is evolved by MHD processes, in particular by the effect of MHD turbulence induced by magnetorotational instability (MRI) (84) or viscous process (see § 2.2). During the MHD or viscous evolution of the disk, a short gamma-ray burst (sGRB) jet may be launched from the vicinity of the BH by pair-annihilation processes of neutrinos emitted from the inner region of the disk (85, 86, 87, 88, 89, 90, 91) and/or by the effect of strong magnetic fields such as the Blandford-Znajek mechanism (92, 93, 94, 95). The viscous angular momentum transport process also drives mass ejection in the viscous timescale of the disk (see § 3 for details).

In the case of MNS formation, the MNS's evolution is determined by several processes. Soon after its formation, the gravitational torque associated with nonaxisymmetric structure of the merger remnant plays an important role for transporting angular momentum from the MNS to the surrounding matter (e.g., Ref. (77)). This process reduces the angular momentum of the MNS. If it is marginally stable against gravitational collapse, the MNS collapses to a BH due to this process in $\sim 10\,\mathrm{ms}$. The resulting system is a spinning BH of $\chi \sim 0.6$–0.7 surrounded by a disk of mass 10^{-2}–$10^{-1} M_\odot$ (e.g., Refs. (50, 55)).

On a longer timescale, viscous effects resulting from MHD turbulence are likely to play a key role in the evolution of the MNS (96, 97, 67). At its formation, the MNS is differentially rotating. Furthermore, it should be strongly magnetized and in an MHD turbulence state exciting a turbulent viscosity, because a velocity-shear layer is formed at the contact surfaces of the merging two neutron stars and the Kelvin-Helmholtz instability occurs (98, 40, 41, 99). This instability generates a number of small-size vortexes near the shear layer, and consequently, magnetic fields are wound up by the vortex motion, which enhances the magnetic-field strength on a timescale much shorter than the dynamical timescale of the system, $\sim 0.1\,\mathrm{ms}$. Note that the growth timescale of the Kelvin-Helmholtz instability (100) is $\tau_{\mathrm{KH}} \sim 10^{-7}(\lambda/1\,\mathrm{cm})\,\mathrm{ms}$ for the wavelength λ because the typically velocity at the onset of merger is $\sim 10^{10}\,\mathrm{cm/s}$. Because of the presence of the differential rotation and turbulent viscosity, the angular momentum in the MNS should be transported outward, and as a result, the MNS is likely to settle to a rigidly rotating state (96, 97, 67). Simultaneously, a massive disk surrounding the MNS is formed because of the angular momentum transport. If this angular momentum transport significantly weakens centrifugal force in its central region, the MNS could collapse to a BH. Using the α-viscous prescription

for the turbulent viscosity (101), one can estimate the viscous timescale as

$$\tau_{\mathrm{vis,MNS}} \approx 20\,\mathrm{ms} \left(\frac{\alpha_{\mathrm{vis}}}{10^{-2}}\right)^{-1} \left(\frac{c_s}{c/3}\right)^{-1} \left(\frac{R}{15\,\mathrm{km}}\right)^2 \left(\frac{H}{10\,\mathrm{km}}\right)^{-1}, \tag{1}$$

where α_{vis} is the dimensionless viscous parameter, c_s is the sound velocity, c is the speed of light, R is the equatorial radius of the MNS, and H is the maximum size of the turbulent vortex. If a turbulent state is sufficiently developed, then α_{vis} will become of the order 10^{-2} according to the latest results of high-resolution MHD simulations for accretion disks (102, 103, 104).

If the lifetime of the MNS is longer than $\tau_{\mathrm{vis,MNS}}$ (i.e. MNS mass is not very large), then it will be evolved through the viscous accretion from the disk and cooling by neutrino emission (67). The viscous timescale of the disk is written approximately as

$$\tau_{\mathrm{vis,disk}} \approx 0.5\,\mathrm{s} \left(\frac{\alpha_{\mathrm{vis}}}{10^{-2}}\right)^{-1} \left(\frac{c_s}{c/10}\right)^{-1} \left(\frac{R_{\mathrm{disk}}}{50\,\mathrm{km}}\right) \left(\frac{H/R_{\mathrm{disk}}}{1/3}\right)^{-1}, \tag{2}$$

where R_{disk} is the typical disk radius. The neutrino cooling timescale for MNSs is

$$\tau_\nu \approx \frac{U}{L_\nu} = 10\,\mathrm{s} \left(\frac{U}{10^{53}\,\mathrm{erg}}\right) \left(\frac{L_\nu}{10^{52}\,\mathrm{erg/s}}\right)^{-1}, \tag{3}$$

where U is the thermal energy of the MNS and L_ν is the total neutrino luminosity. Note that at the formation of the MNS, $L_\nu \gtrsim 10^{53}\,\mathrm{erg/s}$ (34, 38, 37, 52), because shock heating at merger significantly increases its temperature, but in $\sim 100\,\mathrm{ms}$ after the formation, L_ν is likely to decease to $\lesssim 10^{53}\,\mathrm{erg/s}$ (67). Thus, if the viscous accretion onto the MNS or the neutrino cooling has a significant effect and the MNS is marginally stable against gravitational collapse, the MNS would collapse to a BH on either of these timescales.

If the MNS mass is sufficiently low, it will not collapse to a BH in $\sim 10\,\mathrm{s}$. In this case, the MNS is likely to settle to a rapidly and rigidly rotating cold neutron star (a so-called SMNS). The maximum mass of the SMNS is by $\sim 0.4 M_\odot$ increased by the rigid rotation if it is rotating nearly with the maximum angular velocity, $\sim \sqrt{GM_{\mathrm{MNS}}/R^3}$ (105, 106), where M_{MNS} denotes gravitational mass of the MNS and G is the gravitational constant. For example, if the maximum mass of a cold spherical neutron star is $2.2 M_\odot$, then the maximum mass of the SMNS would be $\sim 2.6 M_\odot$, so that the self gravity of the SMNS could be sustained. However, because a SMNS formed in merger is magnetized, its rotational kinetic energy is subsequently dissipated through the magnetic dipole radiation if a force-free magnetic field is established outside the SMNS. Assuming the presence of dipole magnetic radiation with the luminosity L_{B}, the spin-down timescale of the SMNS is

$$\tau_B \approx \frac{T_{\mathrm{rot}}}{L_{\mathrm{B}}} \approx 650\,\mathrm{s} \left(\frac{B_p}{10^{15}\,\mathrm{G}}\right)^{-2} \left(\frac{M_{\mathrm{MNS}}}{2.5 M_\odot}\right) \left(\frac{R}{15\,\mathrm{km}}\right)^{-4} \left(\frac{\Omega}{7000\,\mathrm{rad/s}}\right)^{-2}, \tag{4}$$

where $T_{\mathrm{rot}}(\sim 0.3 M_{\mathrm{MNS}} R^2 \Omega^2)$ is rotational kinetic energy, B_p is the magnetic-field strength of the SMNS pole, and Ω is the angular velocity of the SMNS. Here, we have assumed that the magnetic-field strength would be significantly enhanced at merger. This estimate shows that the rotational kinetic energy could be dissipated in $\sim 10^3\,\mathrm{s}$. After the dissipation of its rotational kinetic energy, the SMNS should collapse to a BH.
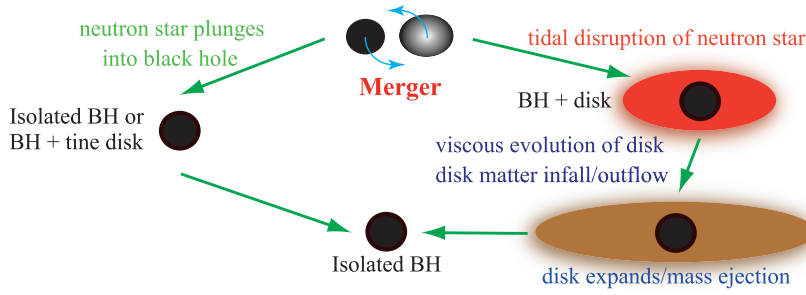
Figure 2

A summary for the merger and post-merger evolution of BH-NS binaries. This system has two possible fates; the neutron star is tidally disrupted or not by the companion BH. For the case of tidal disruption, the remnant is a spinning BH surrounded by a disk. The evolution process of the BH-disk system is essentially the same as that for binary neutron star mergers.

2.2. Black Hole-Neutron Star Binaries

Figure 2 summarizes the possible remnants and their evolution processes expected for mergers of BH-NS binaries. BH-NS binaries have two possible fates: Either the neutron star is tidally disrupted before it is swallowed by the BH or it is swallowed by the BH without disruption (70). For the latter case, essentially disk is not formed and no matter is ejected, and there is no or weak EM emission.

Tidal disruption of a neutron star occurs if the tidal force by BHs is stronger than the self-gravity of the neutron star. Assuming Newtonian gravity, the condition is approximately written as $GM_{BH}R_1/r^3 > GM_{NS}/R_1^2$. Therefore,

$$\left(\frac{GM_{BH}}{c^2 r}\right)^{3/2} \left(\frac{M_{NS}}{M_{BH}}\right) \left(\frac{R_1}{Gc^{-2}M_{NS}}\right)^{3/2} > 1, \tag{5}$$

where r is the orbital separation, M_{BH} and M_{NS} are the mass of the BH and neutron star, and R_1 is the semi major axis of the neutron star. R_1 is by a factor of ~ 1.5 larger than the neutron-star radius, R_{NS}, at the onset of tidal disruption. For tidal disruption, the condition of Eq. 5 should be satisfied before the neutron-star orbit reaches the innermost stable circular orbit (ISCO) around the BH, at which $r = \xi Gc^{-2}M_{BH}$, where $\xi = 6$ for non-spinning BHs and $\xi = 1$ for extremely rapidly spinning BHs (which is corotating with the binary orbit). Here, we have assumed that $Q = M_{BH}/M_{NS}$ is large enough that we can ignore the tidal deformation effect of neutron stars to the orbital motion. Then, we can rewrite Eq. 5 as

$$\left(\frac{\xi}{6}\right)^{-3/2} \left(\frac{Q}{7}\right)^{-1} \left(\frac{R_1}{10Gc^{-2}M_{NS}}\right)^{3/2} > 3.25. \tag{6}$$

We note that $Gc^{-2}M_{NS} \approx 2.0(M_{NS}/1.35M_\odot)\,$km. This condition indicates that tidal disruption occurs for low values of ξ (i.e., for rapidly spinning BHs) or for low values of Q, if the BH spin is not very large. Since the value of Q is likely to be higher than ≈ 4 for the typical neutron-star mass of 1.3–$1.4M_\odot$, we find that a high-spin BH is needed for tidal disruption of neutron stars.

Numerical-relativity simulations have shown that for the case in which a neutron star is tidally disrupted, an accretion disk is subsequently formed around a spinning BH (107, 108, 33, 109, 110, 111, 35, 44, 46, 47, 36, 48, 112, 113, 42, 53, 54). Also, a fraction of

neutron-rich matter is ejected from the system (see § 3.2) (44, 113, 53, 54). The disk mass, M_{disk}, depends strongly on Q, R_{NS}, and BH spin. Among these three parameters, the BH spin is the most substantial. For example, for a dimensionless BH spin, $\chi = 0.75$, with $R_{\mathrm{NS}} \approx 13\,\mathrm{km}$, M_{disk} can be $\sim 10\%$ and 20% of M_{NS} for $Q = 7$ and 3, respectively (113). For $\chi = 0.9$, M_{disk} is $\sim 20\%$ of M_{NS} for $Q = 7$ and $R_{\mathrm{NS}} \approx 13\,\mathrm{km}$ (44). Loverace et al. find that for $\chi = 0.97$, with $Q = 3$ and $R_{\mathrm{NS}} \approx 14\,\mathrm{km}$, M_{disk} can be $\sim 0.5 M_{\mathrm{NS}}$ (46).

Next, we turn our attention to MHD/viscous evolution of a disk surrounding a rapidly spinning BH after a BH-NS merger. Such an accretion disk has nearly Keplerian motion (i.e., differential rotation) and should have magnetic fields originating in the neutron star's magnetic fields. Thus, the disk is unstable to the MRI, and as a result, it is likely to be in a turbulent state (84), enhancing turbulent viscosity (102, 103, 104). Therefore, the BH accretion disk evolves through the viscous process on the timescale of Eq. 2. Specifically, viscous heating and angular momentum transport, together with neutrino cooling, are the key processes. Through viscous angular momentum transport, matter in the inner part of the disk falls into the BH while its outer part gradually expands along the equatorial plane. Viscous heating increases the temperature of the disk to $\sim$ 1–10 MeV, leading to appreciable neutrino emission (86, 87, 88, 89, 90, 91, 66, 68). If the density of the disk is sufficiently high, $\gtrsim 10^{11}\,\mathrm{g/cm^3}$, then the optical depth to neutrinos is large enough to avoid free-streaming escape, suppressing neutrino emissivity. In this phase, the temperature of the disk is determined by the condition that the timescales of the neutrino cooling and viscous heating approximately agree with each other. Throughout the evolution of the system, the density of the disk decreases because of the mass infall into the BH together with expansion of the disk by the viscous angular momentum transport. Then, the optical depth of the disk to neutrinos decreases (61). In this later phase, adiabatic expansion of the disk (not the neutrino cooling) as well as infall into the BH becomes the primary cooling process while viscous heating is always the dominant heating process. This late-phase adiabatic expansion of the disk eventually drives mass ejection (see § 3.3).

The vicinity of spinning BHs is likely to be the site for high-energy phenomena for two reasons. First, the temperature of disks near BHs can be quite high $\gtrsim$ 10 MeV, and hence high-energy neutrinos are copiously emitted. Because of the high temperature, the disks can be geometrically thick, so an appreciable fraction of neutrinos are emitted toward the rotational axis of the spinning BHs. This enhances the pair annihilation of neutrinos and their anti-neutrinos, leading to pair production of electrons and positrons, which could subsequently produce γ-rays through pair annihilation. If the total energy of electrons and positrons is high enough, they could be the engine for driving an sGRB (85, 86, 87, 88, 89, 90, 91, 66)

Second, as mentioned above, the BH accretion disk is likely to be strongly magnetized due to the MRI. If the resulting magnetic pressure is high enough to blow off the matter in the vicinity of the disk, then MHD outflow could be driven. Subsequently, poloidal magnetic fields are likely to be formed near the spinning BH and some of the magnetic field lines would penetrate the BH horizon. In such a magnetic-field configuration, the rotational kinetic energy of the spinning BH could be extracted by the Blandford-Znajek mechanism (92). If the extracted energy is well collimated toward the polar direction and leads to relativistic jets, an sGRB may be produced (42, 93, 94, 95).
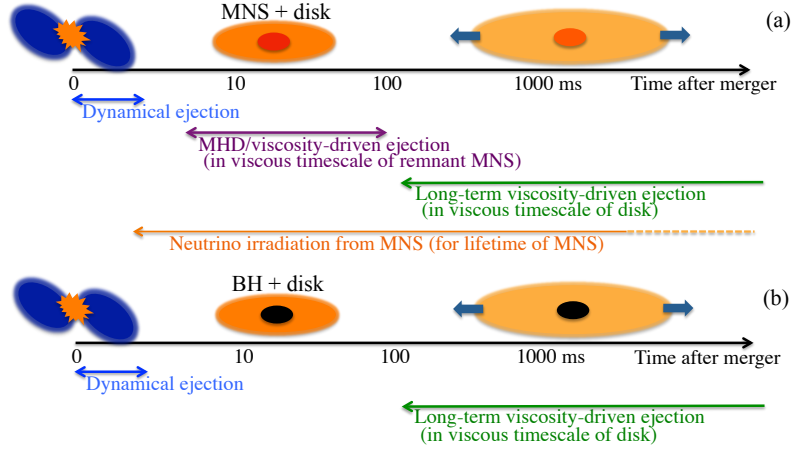
Figure 3

Mass ejection mechanisms during and after merger of binary neutron stars. Soon after the onset of merger, dynamical mass ejection occurs in the timescale of ($\lesssim 10\,\mathrm{ms}$). Subsequently, MHD- or viscosity-driven mass ejection occurs. The panel (a) shows a possible mass ejection history for the MNS formation case. Since both the MNS and surrounding disk are differentially rotating and strongly magnetized, MHD turbulence is likely to be generated. Then, the viscous effect in the MNS can be the cause of the early viscosity-driven mass ejection in $\lesssim 100\,\mathrm{ms}$ after merger. Subsequently, the viscous effect in the disk can drive mass ejection. Because of the presence of the MNS, which is a strong neutrino emitter, the neutrino irradiation plays a key role for determining the electron fraction of the ejecta. The panel (b) shows a possible mass ejection history for the prompt BH formation, for which only dynamical mass ejection and viscosity-driven mass ejection from the disk can occur, and the neutrino irradiation plays a minor role.

3. MASS EJECTION FROM NEUTRON-STAR MERGERS

During and after neutron-star mergers, neutron-rich matter can be ejected. First, at merger, the matter is dynamically ejected on the timescale of $\lesssim 10\,\mathrm{ms}$. Such mass ejection is referred to as the dynamical mass ejection. Second, the mass ejection can proceed from the merger remnant through MHD or viscous processes. Such mass ejection is referred to as the post-merger mass ejection (see Fig. 3 for these mass ejection processes). In the following subsections, we describe these two mass ejection mechanisms. We focus on the mass, velocity, and electron fraction of the ejecta because these quantities determine the property of EM counterparts associated with the ejecta.

3.1. Dynamical Mass Ejection from Binary Neutron Stars

In the mergers of binary neutron stars, strong shock waves are generated by the high-velocity ($\sim 0.2c$) collision. In the shock waves, kinetic energy associated with the neutron stars' plunging motion is converted to thermal energy, which enhances thermal pressure and induces the ejection of the shocked matter. Also, if an MNS is the merger remnant, it is initially highly nonaxisymmetric and oscillating. Such nonaxisymmetric MNS gravitationally exerts torque on the matter surrounding it and induces quick angular-momentum transport. Through this process, the matter in the outer part of the system gains energy sufficient for ejection from the system. These two mechanisms drive dynamical mass ejec-

tion. The timescale of these processes is $\lesssim 10$ ms. Gravitational torque causes matter to be ejected primarily in the equatorial direction, while shock heating causes it to be ejected in a less anisotropic manner.

3.1.1. Mass. The mass of dynamical ejecta depends on the total mass, m, and mass ratio, $q = m_2/m_1$, of binary neutron stars. For $m > M_{\mathrm{thr}}$, a BH is promptly formed after the onset of merger (Fig. 1). For $q \approx 1$, $\geq 99.9\%$ of the neutron-star matter is swallowed by the formed BH (74, 75), and appreciable mass ejection cannot be expected. If the mass ratio is different from unity, a fraction of matter may be dynamically ejected (43, 55, 56). In this case, tidal torque exerted by a deformed compact object collapsing to a BH is what drives the dynamical mass ejection. Numerical-relativity simulations show that $q \lesssim 0.8$ is necessary for dynamical mass ejection with mass $\geq 10^{-3} M_\odot$.

In the case of MNS formation, the dynamical ejecta mass depends strongly on the neutron-star EOS as well as m for the following reason: For stiff EOSs (i.e., large neutron-star radii), the velocity of two neutron stars at merger is relatively small because the minimum orbital separation is large; thus, the shock heating efficiency and oscillation kinetic energy of the remnant MNS are relatively small. This results in a small dynamical ejecta mass. For practically the same reason, the dynamical ejecta mass depends on the total mass of the system, because for high total mass, the shock heating efficiency and kinetic energy of the MNS oscillation can be large, resulting in a high dynamical ejecta mass. Numerical-relativity simulations show that for EOSs with $R_{\mathrm{NS}} \gtrsim 13$ km or for $m \lesssim 2.6 M_\odot$, the dynamical ejecta mass is of the order of $10^{-3} M_\odot$ for $q \sim 1$. Only for $q \lesssim 0.8$, the dynamical ejecta mass can be $\gtrsim 0.005 M_\odot$ (43, 55, 56). By contrast, for $R_{\mathrm{NS}} \lesssim 12$ km with $m \gtrsim 2.7 M_\odot$, the dynamical ejecta mass could be $\sim 0.01 M_\odot$ depending weakly on q. Thus, the dynamical ejecta mass contains information about the neutron star EOS.

3.1.2. Velocity. Since the dynamical mass ejection occurs from the vicinity of merged objects of scale R, the velocity of the ejecta should be of the order of its escape velocity, i.e., $\sim \sqrt{Gm/R} \approx 0.44c(m/2.6M_\odot)^{1/2}(R/20\,\mathrm{km})^{-1/2}$. Numerical-relativity simulations show that the typical average velocity is 0.15–0.25c for the case of MNS formation (e.g., Ref. (43)). For the prompt formation of a BH from highly asymmetric binaries, the average velocity of ejecta is higher $\sim 0.3c$, because the dynamical mass ejection proceeds only for matter in the vicinity of the object collapsing to a BH by a tidal torque exerted.

In the case of the MNS formation, the dynamical mass ejection is induced in part by shock heating. For the shocked ejecta component, a fraction of matter could have a relativistic speed up to $\sim 0.8c$ and, in addition, the ejecta morphology is quasi-spherical (43, 45). Such high-velocity ejecta can generate a characteristic observational feature during the interaction with interstellar matter (ISM); cf. §4.3 (58, 114).

3.1.3. Electron fraction. The electron fraction (Y_e) of ejecta is one of the key quantities for determining the abundance of elements synthesized by r-process nucleosynthesis (15, 16, 59, 115). The abundance pattern of the r-process elements is crucial for determining the opacity of EM emission from the merger ejecta (13, 17, 18, 116, 117).

Because the typical Y_e value for neutron stars is quite low, 0.05–0.1, Y_e of the dynamical ejecta would also be low if the neutron-star matter is ejected without undergoing weak interaction processes. However, the dynamical ejecta could be influenced strongly by the weak processes. First, shock heating at merger and during subsequent evolution of the

merger remnant increases the matter temperature beyond $10\,\mathrm{MeV}$ (34, 38). In such a high-temperature environment, the electron-positron pair creation is enhanced. As a result, neutrons easily capture positrons via $n + e^{+} \rightarrow p + \bar{\nu}_e$. Because the luminosities and average energies of electron neutrinos and electron antineutrinos are roughly equal, and because the average energies are larger than the neutron-proton mass difference, the Y_e value of the initially neutron-rich material is driven toward $1/2$. Thus, in the presence of many positrons produced by pair creation, the fraction of protons and Y_e are increased (i.e., the neutron-richness is reduced) (118).

In the presence of an MNS that is a strong neutrino emitter, the neutrino irradiation to the matter surrounding the MNS could significantly change its composition. Since neutrons and protons absorb neutrinos via $n + \nu_e \rightarrow p + e^{-}$ and $p + \bar{\nu}_e \rightarrow n + e^{+}$, respectively, the fractions of neutrons and protons tend to equilibrate. Because the luminosity and average energy of electron neutrinos and electron antineutrinos from the MNS are not significantly different, the fractions of protons and neutrons approximately approach the same values (i.e., Y_e approaches $1/2$ and the neutron-richness is significantly reduced).

As mentioned above, there are two engines driving dynamical mass ejection: shock heating and tidal torque. Both effects play an important role in the case of MNS formation. On one hand, shock heating and neutrino irradiation from the MNS increase Y_e for a large fraction of ejecta. On the other hand, matter ejected by tidal torque does not always undergo the weak interaction: If a fraction of the matter is ejected by tidal torque without undergoing shock heating and neutrino irradiation, the low-Y_e state is preserved. Therefore, the dynamical ejecta for the MNS formation case in general has components with a wide range of Y_e between ~ 0.05 (i.e., the original value in neutron stars) and ~ 0.5, and if the weak-interaction effect is not significant, a large fraction of ejecta has low values of Y_e.

In the case of prompt BH formation, most of the shock-heated matter is swallowed by the BH, and a strong neutrino irradiation source such as an MNS is absent. For asymmetric binaries, a fraction of matter is ejected by the effect of tidal torque, but in this case, the weak interaction does not play a role; therefore, Y_e of the ejecta is low, $Y_e \lesssim 0.1$.

3.2. Dynamical Mass Ejection from Black Hole-Neutron Star Binaries

If a neutron star is tidally disrupted by its companion BH, a fraction of the neutron-star matter is ejected. In contrast to binary neutron star mergers, for BH-NS binaries, only the tidal effect plays an important role in the dynamical mass ejection.

Broadly speaking, the mass of dynamical ejecta is determined by how the tidal disruption of a neutron star proceeds. If a neutron star is tidally disrupted far from the ISCO of its companion BH, a fraction of the neutron-star matter remains outside the BH horizon after merger. Numerical-relativity simulations show that for such cases, typically $\sim 20\%$ of the matter located outside the horizon escapes from the system as ejecta (113). Thus, larger disk mass results in larger dynamical ejecta mass, up to $\sim 0.1 M_{\odot}$ at maximum. Of course, if neutron stars are not tidally disrupted, the dynamical ejecta mass is absent. Thus, the dynamical ejecta mass is in the range of 0–$0.1 M_{\odot}$ for BH-NS binaries.

The average velocity of dynamical ejecta is determined by the velocity scale of the neutron star at tidal disruption, i.e., 0.2–$0.3c$. Again, high-velocity matter can be present because a part of ejecta comes from the vicinity of the BH horizon. In particular, in the case of a spinning BH, the radius of the event horizon is small, so the fraction of the high-velocity component can be increased.

Because dynamical ejecta is launched predominately by tidal torque and weak-interaction processes such as neutrino irradiation play minor roles in the ejecta, the Y_e value of the dynamical ejecta is always low ($\lesssim 0.1$) (36, 48, 54). This result is highly different from that in binary neutron star mergers resulting in an MNS (see § 3.1).

3.3. Viscosity-Driven Mass Ejection from Merger Remnants

In general, after merger of neutron-star binaries, an MNS or a BH surrounded by a disk is formed. At their formation, both the MNS and disk are differentially rotating and likely to be strongly magnetized; therefore, MHD turbulence should be induced. Turbulent viscosity could then be strongly enhanced as mentioned in § 2. This viscous effect induces the so-called viscosity-driven mass ejection (61, 62, 65, 67). We describe this mechanism in the following subsections.

3.3.1. Mass ejection driven by the viscous effect of massive neutron stars.
First, we discuss the case of MNS formation for binary neutron star mergers. If MHD turbulence develops and the resulting turbulent viscosity is sufficiently high, the differential rotation energy of the remnant MNS could be the energy source of mass ejection. The angular momentum is transported in the MNS on the timescale described by Eq. 1. As a result, the angular velocity profile of the MNS is rearranged into a rigidly rotating state. The density and pressure profiles also change during this transition because the centrifugal force is rearranged. Here, the total rotational kinetic energy of an MNS estimated by $T_{\rm kin} \sim I\Omega^2/2 \sim 0.3 M_{\rm MNS} R^2 \Omega^2$ (105, 106) is quite large:

$$T_{\rm kin} \sim 2 \times 10^{53} \left(\frac{M_{\rm MNS}}{2.6 M_\odot} \right) \left(\frac{R}{15\,{\rm km}} \right)^2 \left(\frac{\Omega}{7000\,{\rm rad/s}} \right)^2 \; {\rm erg}. \tag{7}$$

This energy could be redistributed in the viscous timescale of ~ 10–$20\,{\rm ms}$. In association with the change of the density profile, strong density waves are generated. The density waves subsequently propagate outward, and consequently, shocks are generated in the disk. The shock waves sweep matter into the disk and envelope, which subsequently undergoes outgoing motion. If the energy of a fraction of the matter becomes high enough, mass ejection could occur.

Because the power of the density waves depends on the strength of the viscous effect, the ejecta mass in this process depends on the viscous parameter. A numerical-relativity simulation shows that the eject mass is $\sim 0.01 M_\odot (\alpha_{\rm vis}/0.02)$ (67). The ejecta is launched originally from the vicinity of the MNS. Therefore, the typical velocity of this ejecta component agrees approximately with the escape velocity of the MNS, i.e., $\sim 0.15c$. The electron fraction of this component is widely distributed as in dynamical ejecta. However, the low-Y_e components are absent because the neutrino irradiation from the MNS is strong enough to increase it to $Y_e \gtrsim 0.2$, yielding values between 0.2 and 0.5.

3.3.2. Mass ejection driven by the viscous effect of disks.
For the longer-term evolution, viscous heating and angular momentum transport in the disk play important roles in mass ejection regardless of the formation of MNS or BH. In early disk evolution, thermal energy generated by viscous heating is consumed primarily by neutrino emission. This stage is described by a neutrino-dominated accretion disk (87) with a fraction of the outflow toward the polar direction driven by neutrino heating including neutrino-antineutrino pair annihi-

Table 1 $M_{\rm ej,dyn}$ and $M_{\rm ej,vis}$: dynamical and post-merger ejecta mass in units of $M_\odot$, $Y_{e,\rm dyn}$: Y_e of dynamical ejecta, $Y_{e,\rm vis}$: Y_e of post-merger ejecta, $\langle v_{\rm ej} \rangle$: average velocity of dynamical ejecta in units of c. Low-m, Mid-m, and High-m imply that the remnants soon after the merger are SMNS, HMNS, and BH. BNS denotes binary neutron star.

Type of binary	Remnant	$M_{\rm ej,dyn}$	$M_{\rm ej,vis}$	$Y_{e,\rm dyn}$	$Y_{e,\rm vis}$	$\langle v_{\rm ej} \rangle$
Low-m BNS	SMNS	$O(10^{-3})$	$O(10^{-2})$	0.05–0.5	0.3–0.5	0.15
Mid-m BNS (stiff EOS)	HMNS	$O(10^{-3})$	$O(10^{-2})$	0.05–0.5	0.2–0.5	0.15
Mid-m BNS (soft EOS)	HMNS	$\sim 10^{-2}$	$O(10^{-2})$	0.05–0.5	0.2–0.5	0.20
High-m BNS ($q \sim 1$)	BH	$< 10^{-3}$	$< 10^{-3}$	—	—	—
High-m BNS ($q \ll 1$)	BH	$O(10^{-3})$	$\lesssim 10^{-2}$	0.05–0.1	0.05–0.3	0.30
BH-NS	BH	0–0.1	0–0.1	0.05–0.1	0.05–0.3	0.30

lation heating. In the later stages, the mass, density, and temperature of the disk decrease because of the outflow and accretion onto the MNS. The decrease of the temperature, T, causes a reduction in the neutrino emissivity because of its strong dependence on T, which is approximately proportional to T^6 (86). Then, the viscous heating is used primarily for the adiabatic expansion of the disk toward the equatorial direction. The continuous viscous heating causes the disk matter to eventually escape from the system as ejecta.

Because viscous mass ejection from a disk should occur regardless of the viscous parameter (for reasonably large values of $\alpha_{\rm vis}$), ejecta mass in this process depends weakly on its value. Numerical simulations show that the ejecta mass could be a substantial fraction (more than half) of the disk mass of 0.01–$0.1 M_\odot$ for the presence of an MNS (62, 63, 67). For the presence of a BH, the mass falling into the BH is larger than that of the outflow. However, numerical simulations for disks around spinning BHs show that $\sim 20\%$ of the disk mass can be ejected (61, 65). If the matter is ejected efficiently by MHD processes, this fraction may be increased by a factor of two (66, 68).

The ejecta in this mechanism is launched primarily from the outer part of disks. If the mass ejection occurs at a radius of $r \gtrsim 100 G c^{-2} M$ ($M = M_{\rm MNS}$ or $M_{\rm BH}$), then the characteristic velocity would be $\lesssim 0.1c$. Thus, the typical velocity of this ejecta component is smaller than that for dynamical ejecta and early viscosity-driven ejecta powered by the MNS.

The values of Y_e within the dynamical ejecta vary widely. However, the low end depends strongly on the presence or absence of the MNS, which can be the strong neutrino irradiation source (62). In the presence of the MNS, the low end of Y_e could be ~ 0.3 (63, 67), whereas in its absence (i.e., in the presence of a BH), low Y_e values are preserved for a substantial fraction of the ejecta (62, 65). The reasons are that the disk is dense and electrons are degenerate, resulting in the low Y_e state in the disk, and that the weak interaction does not play an important role because neutrino irradiation is weak in this case (61).

3.4. Summary of Ejecta

Table 1 summarizes the typical properties of ejecta, showing that the ejecta quantities depend strongly on the binary parameters, so that the observational features of the EM emission (in particular kilonova emission: see §4.2) can be different for each merger event.

4. ELECTROMAGNETC COUNTERPARTS OF NEUTRON-STAR MERGERS

Neutron star mergers eject a substantial amount of neutron-rich material, in which r-process nucleosynthesis robustly occurs. Subsequently, synthesized radioactive elements shine, in particular, as a kilonova (macronova). In addition, the ejecta have large kinetic energy with mildly-relativistic velocities, leading to a long-lasting synchrotron remnant. In the following subsections, we first summarize the general properties of r-process nucleosynthesis in mergers, then describe models of kilonovae and synchrotron remnants as promising EM signals.

4.1. r-Process Nucleosynthesis and Ejecta Opacity

As described in § 3, dense neutron-rich matter is generally ejected in neutron-star mergers. The neutron-rich ejecta can subsequently synthesize heavy elements through r-process nucleosynthesis,, that is, by rapid neutron capture, where the capture timescale is typically shorter than the β-decay timescales (118).

In the r-process nucleosynthesis, the abundance of elements synthesized depends primarily on the neutron richness, entropy, and density (118). Among these properties, the neutron richness (i.e., Y_e) is the key quantity in mergers. Numerical calculations show (15, 16) that for ejecta only with neutron-rich matter of $Y_e \lesssim 0.1$, r-process elements with mass number larger than $A \gtrsim 120$ (i.e., the elements in the so-called second and third peaks) are robustly synthesized. In this case, the mass fraction of elements with $A \lesssim 120$ is quite small. This finding implies that for BH-NS mergers and binary neutron star mergers collapsing promptly to a BH, predominantly heavy r-process elements are synthesized. By contrast, from ejecta with $Y_e \gtrsim 0.25$, heavy elements with $A \gtrsim 130$ (e.g., lanthanides) are not synthesized (16, 59, 115). In the presence of a wide range of Y_e values in ejecta, r-process elements with a wide mass range are synthesized, as was first pointed out in Ref. (59). As mentioned in § 3, for mergers of binary neutron stars leading to an MNS, matter with a wide range of Y_e values, 0.05–0.5 (see Table 1), is ejected; thus, r-process elements with $A \gtrsim 70$ are synthesized simultaneously.

4.2. Kilonova (Macronova)

Kilonovae are uv-optical-IR transients powered radioactively by r-process elements freshly synthesized in merger ejecta.

4.2.1. Radioactive heating.
The radioactive decay channels of neutron-rich heavy elements are (i) β-decay, (ii) α-decay, and (iii) fission. The specific heating rate of the second and third of these channels depends sensitively on the abundance of superheavy nuclei ($A \geq 210$ for alpha decay and $A \geq 250$ for fission). In the following, we describe the heating process for each channel.

β-decay: β-unstable nuclei decay toward the stability valley without changing the atomic mass number. Because the number of nuclei is conserved for each atomic mass number, the decay rate is approximately proportional to t^{-1}, where radioactive species with mean-lives $\tau \sim t$ predominately contribute to the decay rate at t. The electron energy liberated in each decay generally decreases with the lifetime as $E_e \propto \tau^{-1/5}$ to $\tau^{-1/3}$. Thus, the energy releasing rate in β-decay electrons per unit mass is $\dot{q}_e(t) \propto t^{-6/5}$ to $t^{-4/3}$ (13, 119), which
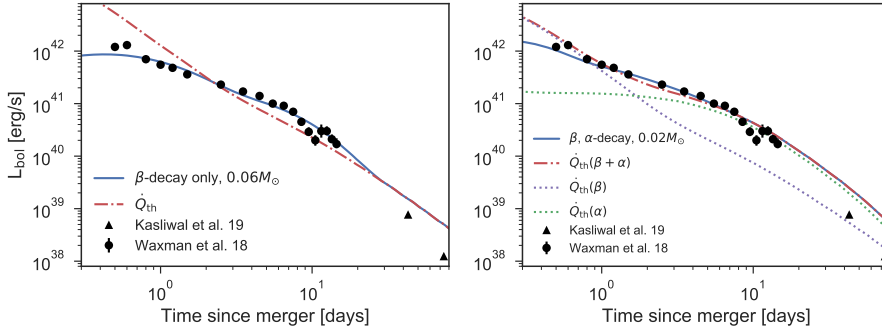
Figure 4

β-decay heating rate and bolometric light curve models for ejecta of the solar r-process abundance with $A \geq 85$ (*left*) and those including α-decay heating (*right*). For the *left* panel, the total r-process mass and the typical ejecta velocity are set to be $0.06M_\odot$ and $0.15c$. The opacity is assumed to be $1\,\mathrm{cm^2/g}$ for $v > 0.15c$ and $7\,\mathrm{cm^2/g}$ for $v \leq 0.15c$. Note that this opacity distribution is phenomenological to fit the bolometric data and somewhat motivated from the models shown in Refs. (133, 134). For the *right* panel, the initial abundance of $A = 222$, 223, 224, and 225 is taken to be $Y_A = 4.0 \times 10^{-5}$, 2.7×10^{-5}, 4.1×10^{-5}, and 2.7×10^{-5}, respectively, corresponding to the DZ31 model presented in Wu et al. (120). The total r-process mass and the typical ejecta velocity are supposed to be $0.02M_\odot$ and $0.1c$ for this case. The opacity is assumed to be $0.1\,\mathrm{cm^2/g}$ for $v > 0.1c$ and $1\,\mathrm{cm^2/g}$ for $v \leq 0.1c$. Also depicted are the observed bolometric light curve data of GW170817 (129) and νL_ν of the late-time Spitzer observations at $4.5\,\mu\mathrm{m}$ (131).

is typically written as

$$\dot{q}_e(t) \approx 3 \cdot 10^9 \,\mathrm{erg\,s^{-1}g^{-1}} \left(\frac{t}{1\,\mathrm{day}} \right)^{-4/3}. \qquad (8)$$

β-decay is often followed by γ-ray emission and the efficiency of the energy release in γ-rays is ~ 0.3–2 times that of $\dot{q}_e(t)$.

α-*decay:* Neutron-rich elements with $210 \leq A \lesssim 254$ increase their proton fraction through β-decay until the point at which they are predominately disintegrated by α-decay. After a number of α-decays and β-decays, they eventually reach stable nuclei with $A < 210$. Each α decay liberates energy of ~ 5–10 MeV. Among the α-unstable elements, ^{222}Rn, ^{223}Ra, ^{224}Ra, ^{225}Ra, and ^{225}Ac are particularly relevant for the kilonova heating rate (120). In a decay chain of these elements, 20–30 MeV is released in total. Nuclei with $222 \leq A \leq 225$ can dominate over the β-decay heating for $t >$ a few days, if the total mass of these elements is $\gtrsim 10^{-3}M_\odot$ (Fig. 4).

Spontaneous fission: Transuranium nuclides with $A \gtrsim 250$ may be disintegrated by spontaneous fission, in which ~ 100–200 MeV is released as kinetic energy of fission fragments. Thus, the energy release of each fission is greater by a factor of $\gtrsim 100$ than in β-decay. Although the Q-value and half-life of spontaneous fission, as well as the abundance of transuranium nuclides synthesized in merger ejecta, are highly uncertain, spontaneous fission could potentially dominate the heating rate at later times of $\gtrsim 10$ day (59, 121, 122, 120). For instance, a notable element is ^{254}Cf, of which the half-life is 60.5 day and the Q-value is 185 MeV (122, 120).

High energy charged particles (electrons, α-particles, and fission fragments) produced

by radioactive decay deposit their kinetic energy to the thermal energy of merger ejecta on the following timescale (123, 124),

$$t_{\mathrm{th}} \approx \left(\frac{\sigma_{\mathrm{st}}(E_i) N v_i}{E_i} \right)^{-1},$$ (9)

where σ_{st} is the stopping power determined predominantly by the collisional ionization and excitation of ions, N is the number density of ions, E_i and v_i are the initial kinetic energy and velocity of a particle, respectively. E_i is typically 0.1–1 MeV for electrons, 5 MeV for α-particles, and 100 MeV for fission fragments. Since the density decreases with time in expanding ejecta, the thermalization time increases and eventually exceeds the expansion time.

The thermalization timescales for beta-, alpha-, and gamma–decay are

$$t_{\mathrm{th},\beta} \sim 30\,\mathrm{day} \left(\frac{M_{\mathrm{ej}}}{0.05 M_\odot} \right)^{1/2} \left(\frac{v_{\mathrm{ej}}}{0.1c} \right)^{-3/2} \left(\frac{E_i}{0.5\,\mathrm{MeV}} \right)^{-1/2},$$ (10)

$$t_{\mathrm{th},\alpha} \sim 45\,\mathrm{day} \left(\frac{M_{\mathrm{ej}}}{0.05 M_\odot} \right)^{1/2} \left(\frac{v_{\mathrm{ej}}}{0.1c} \right)^{-3/2} \left(\frac{E_i}{5\,\mathrm{MeV}} \right)^{-1/2},$$ (11)

$$t_{\mathrm{th},\gamma} \sim 2.4\,\mathrm{day} \left(\frac{\kappa_\gamma}{0.05\,\mathrm{cm^2/g}} \right)^{-1} \left(\frac{M_{\mathrm{ej}}}{0.05 M_\odot} \right)^{1/2} \left(\frac{v_{\mathrm{ej}}}{0.1c} \right)^{-1},$$ (12)

where M_{ej} and v_{ej} denote the mass and typical velocity of the ejecta, and $\kappa_\gamma \approx 0.05\,\mathrm{cm^2/g}$ is the mass absorption coefficient of r-process elements at γ-ray energy of $\sim 1\,\mathrm{MeV}$. Note that the thermalization time for fission fragments, $t_{\mathrm{th,sf}}$, is $\sim 2 t_{\mathrm{th},\alpha}$ (123).

Once $t > t_{\mathrm{th},a}$ ($a = \alpha$, β, γ, sf) is achieved, the thermalization rate becomes lower than the adiabatic cooling rate; therefore, a significant fraction of the radioactive energy is lost adiabatically for charged particles and the γ-ray heating rate declines exponentially. The heating rate is equal to the energy generation rate for $t \ll t_{\mathrm{th},a}$, while, for $t \gtrsim t_{\mathrm{th},a}$, the heating rate deviates from the energy generation rate (129, 124) and goes approximately as $\propto t^{-3}$ for $t \gg t_{\mathrm{th},a}$ (129).

4.2.2. Opacity. The opacity for photons plays an essential role for the light curves and spectra of kilonovae. In kilonovae, the opacity is determined primarily by the bound-bound absorption of heavy elements (125, 18). Notably, the bound-bound absorption opacity of open f-shell elements (lanthanides and actinides) differs significantly from the opacity of others, because open f-shell elements have such a high number of excited levels with relatively low excitation energy that the number of transition lines in the optical and IR bands is greatly enhanced (125, 17, 18). Radiation transfer simulations of merger ejecta show that the mean opacity, κ, is $\gtrsim 10\,\mathrm{cm^2/g}$ for lanthanide-rich ejecta while it is $\sim 0.1\,\mathrm{cm^2/g}$ for lanthanide-free ejecta (125, 17, 18, 116, 126, 127). This finding implies that the Y_e distribution of ejecta, which primarily determines the abundance pattern of r-process elements, is the key for determining the features of kilonovae.

4.2.3. Typical light curve. For merger ejecta, the light curve peaks on a timescale (13)

$$t_{\mathrm{p}} \approx \sqrt{\frac{\kappa M_{\mathrm{ej}}}{4\pi c v_{\mathrm{ej}}}} \approx 10\,\mathrm{day} \left(\frac{\kappa}{10\,\mathrm{cm^2/g}} \right)^{1/2} \left(\frac{M_{\mathrm{ej}}}{0.04 M_\odot} \right)^{1/2} \left(\frac{v_{\mathrm{ej}}}{0.1c} \right)^{-1/2}.$$ (13)

The luminosity and effective temperature are estimated as

$$L_{\mathrm{bol}}(t_{\mathrm{p}}) \approx \dot{Q}_{\mathrm{th}}(t_p) = M_{\mathrm{ej}} \cdot \dot{q}_{\mathrm{th}}(t_p) \approx 4 \cdot 10^{40}\,\mathrm{erg/s}\left(\frac{t_p}{10\,\mathrm{day}}\right)^{-1.3}\left(\frac{M_{\mathrm{ej}}}{0.04 M_{\odot}}\right), \qquad (14)$$

$$T_{\mathrm{eff}}(t_{\mathrm{p}}) \approx \left(\frac{L_{\mathrm{bol}}(t_{\mathrm{p}})}{4\pi\sigma v_{\mathrm{ej}}^2 t_{\mathrm{p}}^2}\right)^{1/4} \approx 2000\,\mathrm{K}\left(\frac{L_{\mathrm{bol,p}}}{4\cdot 10^{40}\,\mathrm{erg/s}}\right)^{1/4}\left(\frac{v_{\mathrm{ej}}}{0.1c}\right)^{-1/2}\left(\frac{t_{\mathrm{p}}}{10\,\mathrm{day}}\right)^{-1/2} \quad (15)$$

where σ is the Stefan-Boltzmann constant. These equations show that lanthanide-free ejecta are brighter, bluer, and peaks earlier than lanthanide-rich ejecta if the mass, velocity, and specific heating rate are the same.

Figure 4 (*left*) shows the β-decay heating rate for the solar r-process abundance pattern with $A \geq 85$ and a bolometric light curve calculated using a simple one dimensional ejecta model, in which κ is assumed to be $1\,\mathrm{cm^2/g}$ for $v > 0.15c$ and $7\,\mathrm{cm^2/g}$ for $v \leq 0.15c$ with $M_{\mathrm{ej}} = 0.06 M_{\odot}$. Note that this opacity distribution is phenomenological to fit the bolometric data and is somewhat motivated from the models presented in, e.g., Refs. (133, 134). Kilonova bolometric light curves have following generic features. The bolometric luminosity is lower than the heating rate in the early phase in which most part of the ejecta is optically thick. When the optical depth becomes below $\approx c/v_{\mathrm{ej}}$, photons in the entire ejecta start diffusing out from the ejecta without significant adiabatic losses. At later times, the ejecta density becomes so low that most of photons in the ejecta diffuse out within one dynamical time thereby the bolometric luminosity approaches approximately the total heating rate.

Figure 4 (*right*) illustrates the case in which α-decay enhances the kilonova heating rate. In the example shown in the figure, the α-decay heating rate of the DZ31 model shown in Ref. (120) is added to the β-decay heating rate. Note that this model predicts the production of much larger amounts of α-unstable nuclei than other nuclear mass models (120). With this model, the ejecta mass of $\approx 0.02 M_{\odot}$ is sufficient to generate bolometric light curve as bright as the light curve with only β-decay and $M_{\mathrm{ej}} \approx 0.06 M_{\odot}$.

4.3. Synchrotron Emission

The interaction of merger ejecta with the surrounding ISM produces a long-lasting synchrotron emission observable in multi-wavelength bands from radio to X-rays (30). Various types of merger ejecta, including dynamical and post-merger ejecta, sGRB jets, and cocoons, can produce such signals. Here, we focus on the signal arising from the dynamical ejecta because it is closely related to the merger dynamics (114, 128).

We estimate the flux from dynamical ejecta by modeling it as a spherical expanding shell with single velocity and neglecting relativistic corrections. An ejecta with kinetic energy, E, and initial velocity in units of c, β_i, expanding in the surrounding ISM of a constant number density, n, is decelerated on the following timescale:

$$t_{\mathrm{dec}} \approx 30\,\mathrm{day}\left(\frac{E}{10^{49}\,\mathrm{erg}}\right)^{1/3}\left(\frac{n}{1\,\mathrm{cm^{-3}}}\right)^{-1/3}\beta_i^{-5/3}. \qquad (16)$$

The ejecta velocity (in units of c), β, is constant for $t < t_{\mathrm{dec}}$ and decreases as $\propto t^{-3/5}$ for

$t \gtrsim t_{\mathrm{dec}}$ during the adiabatic expansion phase. The light curve has a peak at $t \sim t_{\mathrm{dec}}$[1]:

$$F_{\nu,\mathrm{peak}} \approx 3\,\mathrm{mJy}\,\left(\frac{E}{10^{49}\,\mathrm{erg}}\right)\left(\frac{n}{1\,\mathrm{cm}^{-3}}\right)^{(p+1)/4}\left(\frac{\epsilon_B}{0.1}\right)^{(p+1)/4}\left(\frac{\epsilon_e}{0.1}\right)^{p-1}\beta_i^{(5p-7)/2}$$

$$\times \left(\frac{D}{100\,\mathrm{Mpc}}\right)^{-2}\left(\frac{\nu}{1.4\,\mathrm{GHz}}\right)^{-(p-1)/2}, \tag{17}$$

where ϵ_B and ϵ_e are the conversion efficiencies of internal energy of the shocked ISM to magnetic-field energy and accelerated electron energy, respectively, and p is the power-law index for the distribution function of accelerated electrons. The value of p is likely to be 2–3 as inferred from the GRB afterglow and radio-supernova observations. Notably, the peak flux is quite sensitive to the ejecta velocity. For a given ejecta mass, the flux increases with velocity as $\propto \beta^{4.75}$ for $p = 2.5$; therefore, the detecting such signals would prove the velocity profile of merger ejecta.

The above estimate is valid if the following three conditions are satisfied: (i) The self-absorption is negligible ($\nu > \nu_a$), (ii) the observed frequency is above the characteristic synchrotron frequency, ($\nu > \nu_m$), and (iii) the observed frequency is below the synchrotron cooling frequency, ($\nu < \nu_c$). Here, the characteristic synchrotron frequency and the cooling frequency are given, respectively, by

$$\nu_m \approx 1\,\mathrm{GHz}\,\left(\frac{n}{1\,\mathrm{cm}^{-3}}\right)^{1/2}\left(\frac{\epsilon_B}{0.1}\right)^{1/2}\left(\frac{\epsilon_e}{0.1}\right)^2\beta^5, \tag{18}$$

$$\nu_c \approx 10^{14}\,\mathrm{Hz}\,\left(\frac{n}{1\,\mathrm{cm}^{-3}}\right)^{-3/2}\left(\frac{\epsilon_B}{0.1}\right)^{-3/2}\left(\frac{t}{30\,\mathrm{d}}\right)^{-2}\beta^{-3}, \tag{19}$$

and the self-absorption frequency at t_{dec} is estimated by

$$\nu_{a,\mathrm{dec}} \approx 1\,\mathrm{GHz}\,\left(\frac{E}{10^{49}\,\mathrm{erg}}\right)^{\frac{2}{3(p+4)}}\left(\frac{n}{1\,\mathrm{cm}^{-3}}\right)^{\frac{3p+14}{6(p+4)}}\left(\frac{\epsilon_B}{0.1}\right)^{\frac{p+2}{2(p+4)}}\left(\frac{\epsilon_e}{0.1}\right)^{\frac{2(p-1)}{p+4}}\beta_0^{\frac{15p-10}{3(p+4)}}. \tag{20}$$

The above equations show that ν_m and ν_a are typically lower than the radio frequency for sub-relativistic ejecta with $n \lesssim 1\,\mathrm{cm}^{-3}$ and that the cooling break is expected to occur between the optical and X-ray bands.

As discussed in §3.1.2, the velocity of dynamical ejecta is typically $\sim 0.2c$ and can reach up to $\sim 0.8c$. The total kinetic energy is $\sim 10^{50}$–$10^{51}\,\mathrm{erg}$ and kinetic energy in the fast component with $v \gtrsim 0.7c$ is $\sim 10^{47}$–$10^{49}\,\mathrm{erg}$ depending on each mass of the binary and neutron-star EOS (see Fig. 5 and Ref. (58, 114)). Such a velocity distribution results in a relatively flat and years-lasting afterglow light curve.

5. GW170817

The observations of EM counterparts to GW170817 have, for the first time, provided valuable information to test theoretical predictions for mass ejection and associated EM emission. In this section, we summarize the observational features of the EM counterparts and briefly describe theoretical models that are broadly consistent with the observational results.

---

[1]The peak time is longer than t_{dec} when the synchrotron self-absorption is important. Such a delay of the peak can occur for mergers at high ISM densities ($\gtrsim 1\,\mathrm{cm}^{-3}$) and/or low observed frequencies ($\lesssim 1$ GHz).
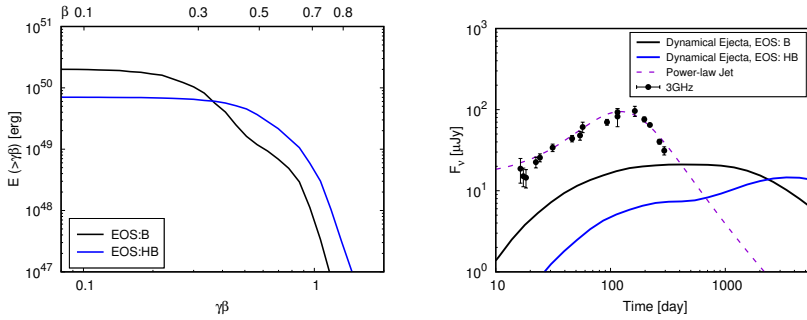
Figure 5

Kinetic energy of dynamical ejecta as a function of four velocity (*left*) and afterglow light curves (*right*). Here the results of dynamical ejecta from binary neutron star mergers with two different EOSs (B and HB) and with mass $m_1 = m_2 = 1.35 M_\odot$ are shown. For computing these light curves, we employ $n = 10^{-3}\,\mathrm{cm}^{-3}$ and microphysics parameters of $\epsilon_B = \epsilon_e = 0.1$ and $p = 2.2$ (114). Also depicted are the observed data of the afterglow in GW170817 at 3 GHz and a light curve for a power-law structured jet model which agrees with the light curve data (142) and the observed superluminal motion (144).
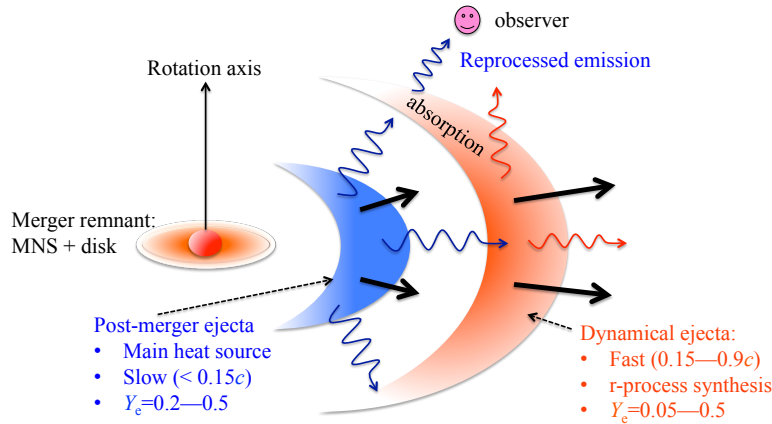
Figure 6

Schematic picture of the ejecta profile for the case that a long-lived MNS is formed as a remnant. The outer falcate component denotes the neutron-rich dynamical ejecta. The inner falcate component denotes the less neutron-rich post-merger ejecta which is slower than the dynamical ejecta. Note that the gravitational-wave observation indicates that the merger remnant of GW170817 is observed along the direction of $\theta \lesssim 30°$ from the rotation axis.

5.1. Kilonova Observation

Figure 4 shows the observed bolometric light curve data of GW170817 (129, 24, 26, 23, 130) and νL_ν of the late-time Spitzer observations at $4.5\,\mu\mathrm{m}$ (131). Here, the late-time Spitzer data are considered approximately as the bolometric luminosity. The observed data are largely consistent with the β-decay heating with $M_{\mathrm{ej}} = 0.06 M_\odot$. Two notable features of this kilonova is that the light curve peaks at $\lesssim 0.5\,\mathrm{d}$ and that the peak luminosity reaches
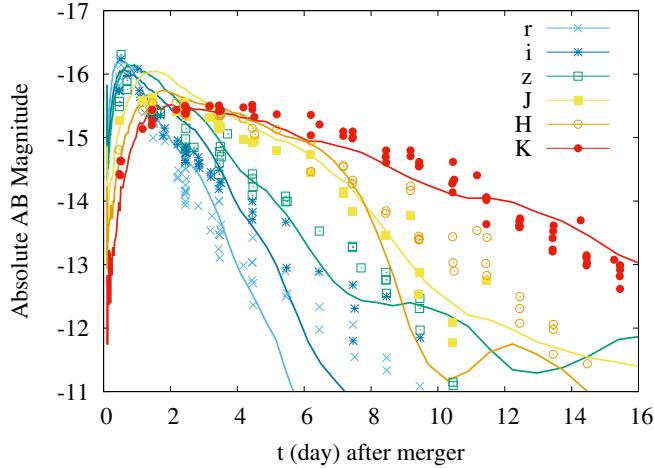
Figure 7

Optical and near infrared (r, i, z, J, H, K bands) light curves of the kilonova associated with GW170817 (points) and theoretical model light curves (curves) based on numerical-relativity simulations (see Fig. 6) assuming the viewing angle of $\approx 25°$ (137). The optical and near infrared data points are taken from Ref. (133). All of the magnitudes are given in AB magnitudes.

$\sim 10^{42}$ erg/s. As shown by Eq. 13., this fact requires that some fractions of the ejecta have a low opacity $\lesssim 1\,\mathrm{cm}^2/\mathrm{g}$, suggesting that there exists a substantial amount of material with a quite low or even zero lanthanide fraction. By contrast, the evolution of the temperature (spectrum) at later times indicates the existence of a lanthanide-rich component. Therefore, the kilonova in GW170817 shows us evidence that merger ejecta has components with a broad range of Y_e (e.g., Fig. 6).

As discussed in §3.1.3, dynamical ejecta has a wide range of Y_e values, but numerical-relativity simulations show that dynamical ejecta mass would be $\lesssim 10^{-2}M_\odot$, which is smaller by a factor of 2 or more than that required to reproduce the observed luminosity. This suggests that the merger remnant would eject $\gtrsim 0.03M_\odot$ from the remnant MNS and/or accretion disk (see §3). The origin of different Y_e components is and how they are spatially distributed are under debate. Several models suggested to date are as follows.

Angular structure model: a lanthanide-free component (blue) and a lanthanide-rich one (red) are angularly separated, for instance, the polar ejecta is lanthanide free (132). Fitting the photometric light curve data of GW170817 leads to the mass of $\approx 0.01M_\odot$ and velocity of $0.3c$ for the blue component and the mass of $\approx 0.04M_\odot$ and velocity of $0.1c$ for the red component (23). Introducing another component results in a better fit to the data (133).

Radial structure mode: the composition (opacity) varies with the ejecta velocity, e.g., the opacity of the fast (slow) moving material is $0.8\,(5)\,\mathrm{cm}^2/\mathrm{g}$, where the two components are separated at $v = 0.1c$ (26, 134).

Temporal variation model: the opacity evolves with time, which is expected from the time variation of the temperature and density of the ejecta (129). The form $\kappa = \kappa_M (t/t_M)^\gamma$ is applied to GW170817 and $\kappa_M \approx 0.3\,\mathrm{cm}^2/\mathrm{g}$, $\gamma \approx 0.6$, and $t_M \approx 1$ d.

Model motivated by numerical relativity: this model employs two (or three) ejecta com-

ponents motivated by the results of numerical-relativity simulations for the merger and post-merger (135, 136, 137). On the basis of the numerical results, the composition is varied both radially and angularly, and non-trivial radiation transfer effects are taken into account.

Figure 7 compares optical and near-IR light curves of the kilonova associated with GW170817 and theoretical curves derived by a radiation-transfer simulation in the background of an ejecta model obtained from numerical-relativity simulations (see Fig. 6 for a schematic figure). This figure illustrates that this model works well (137). However, it is not yet clear whether every kilonova agrees with the prediction of numerical relativity, and comparison with a number of future events is clearly needed to establish the standard picture for kilonovae.

Before closing this section, we note that α-decay and spontaneous fission can potentially enhance the heating rate at late times (see Fig. 4 for α-decay). Although we cannot conclude whether or not such heavy elements play a role for the EM emission of GW170817, the estimated ejecta mass is significantly reduced from $\approx 0.05 M_\odot$ if these decay channels are important. In future events, it may be possible to identify a signature of heavy elements using a bolometric light curve at late times $\gg 10\,\mathrm{day}$.

5.2. Synchrotron Emission and Jet

The X-ray and radio afterglows of GW170817 were discovered at 9 and 16 d after the merger (138, 139). The light curves rise as $\propto t^{0.8}$ until $\approx 150\,\mathrm{days}$ (140) and then both X-ray and radio light curves fall quickly as $\propto t^{-2.2}$ (141, 142). The spectrum of the afterglow is consistent with a single power law, $F_\nu \propto \nu^{-0.6}$, from the radio to X-ray bands (143), which is described well by synchrotron radiation emitted by accelerated electrons in the shocked ISM. The slow rise over a timescale of 150 days is attributed to the fact that the jet structure includes a cocoon component and this feature is quite different from the typical GRB afterglow light curve. It is also remarkable that the fast decline of the light curve agrees with the light curve predicted for the post-jet break regime of collimated jet models. Furthermore, the Very Long Baseline Interferometry observations reveal that the unresolved radio emitting region exhibits a superluminal motion with a Lorentz factor of ≈ 4 (144). These observational features confirm that the afterglow arises from a narrowly collimated relativistic jet with some structure seen from off-axis. The kinetic energy and jet-half opening angle are estimated as $E_j \approx 10^{49}$–$10^{50}\,\mathrm{erg}$ and $\theta_j \lesssim 5^\circ$, respectively (144). Figure 5 shows the light curve of a power-law structured jet model with $E_j \approx 2 \times 10^{49}\,\mathrm{erg}$, $\theta_j \approx 3^\circ$, $n \approx 10^{-3}\,\mathrm{cm}^{-3}$, and the viewing angle $\approx 21^\circ$.

Another important observation that is likely related to the jet is GRB 170817A detected at 1.7 s after the merger (145), which is much weaker than the typical sGRB. This prompt γ-ray emission requires a relativistic motion of the emission region (146). The delay of the γ-ray detection from the merger indicates that the jet should be formed for $\ll 1.7$ s after the merger. On the basis of numerical-relativity simulations, it has been suggested that a relativistic jet may be driven by magnetic fields after an MNS collapses to a BH (147) in a lifetime of $\ll 1.7$ s. The collimation of the jet in GW170817 can be interpreted as follows. The jet interacts with the material ejected around the polar region before the jet breaks out from the ejecta surface. Consequently, the ejecta shocked by the jet form a cocoon which helps collimation of the jet (148, 149, 150). The small opening angle of the jet in GW170817 indicates that an appreciable amount of ejecta is present around the polar region prior to

the jet formation(146).

Figure 5 depicts models for the afterglow light curves arising from dynamical ejecta with an ISM of density $n = 10^{-3}\,\mathrm{cm}^{-3}$. If the microphysics parameters are somewhat optimistic, the radio emission with a flux density of $\approx 10\,\mu\mathrm{Jy}$ may be detectable in near future. Also, we note that for future merger events, this radio emission may be a primary target for the radio-band observation, if the viewing angle of the merger events is sufficiently wide.

ACKNOWLEDGMENTS

LITERATURE CITED

1. J. Abadie *et al.* [LIGO Scientific Collaboration], Nucl. Instrum. Meth. A **624**, 223 (2010).
2. T. Accadia *et al.* [Virgo Collaboration], Class. Quant. Grav. **28**, 025005 (2011) [Erratum-ibid. **28**, 079501 (2011)]:
3. T. Akutsu et al., Prog. Theor. Exp. Phys. **013F01** (2018).
4. B. P. Abbott *et al.*, Phys. Rev. Lett. **119**, 161101 (2017).
5. J. M. Lattimer and D. N. Schramm, Astrophys. J. Lett. **192**, L145 (1974).
6. D. Eichler, M. Livio, T. Piran, and D. N. Schramm, Nature **340** , 126 (1989).
7. F.-K. Thielemann, M. Eichler, I. V. Panov, and B. Wehmeyer, Annu. Rev. Nucl. Part. Sci. **67**, 253 (2017).
8. M. D. Davies, W. Benz, T. Piran, and F. K. Thielemann, Astrophys. J. **431**, 742 (1996).
9. M. Ruffert, H.-Th. Janka, K. Takahashi and G. Schaefer, Astron. Astrophys. **319**, 122 (1997).
10. C. Freiburghaus, S. Rosswog, and F.-K. Thielemann, Astrophys. J. **525**, L121 (1998).
11. S. Rosswog, M. Liebendoerfer, F.-K. Thielemann, M. B. Davies, W. Benz, and T. Piran, Astron. Astrophys. **341** 499 (1999).
12. L.-X. Li and B. Paczhński, Astrophys. J. **507**, L59 (1998).
13. B. D. Metzger, G. Martinez-Pinedo, S. Darbha, E. Quataert, A. Arcones, D. Kasen, T. Thomas, P. Nugent, I. V. Panov, and N. T. Zinner, Mon. Not. Roy. Soc. **406**, 2650 (2010).
14. L. F. Roberts, D. Kasen, W. H. Lee, and E. Ramirez-Ruiz, Astrophys, J. **736**, L21 (2011).
15. S. Goriely, A. Bauswein, and H.-T. Janka, Astrophys. J. Lett. **738**, L32 (2011).
16. O. Korobkin, S. Rosswog, A. Arcones, and C. Winteler, Mon. Not. R. Astron. Soc. **426**, 1940 (2012).
17. J. Barnes and D. Kasen, Astrophys. J. **775**, 18 (2013).
18. M. Tanaka and K. Hotokezaka, Astrophys. J. **775**, 113 (2013).
19. LIGO Scientic Collaboration and VIRGO Collaboration et al., Astrophys. J. **848**, L12 (2017).
20. M. Tanaka et al. Pub. Astron. Soc. Japan **69**, 102 (2017).
21. I. Arcavi et al., Nature **551**, 64 (2017).
22. D. A. Coulter et al., Science **358**, 1556 (2017).
23. P. S. Cowperthwaite et al., Astrophys. J. Lett. **848**, L17 (2017).
24. M. R. Drout et al., Science **358**,1570 (2017).
25. P. A. Evans et al., Science **358**, 1565 (2017).
26. M. M. Kasliwal et al., Science **358**, 1559 (2017).
27. E. Pian, et al., Nature **551**, 67 (2017).
28. S. J. Smartt et al., Nature **551**, 75 (2017).

29. N. R. Tanvir et al., Astrophys. J. Lett. **848**, L27 (2017).

30. E. Nakar and T. Piran, Nature **478**, 82 (2011).

31. M. Shibata, Phys. Rev. D **60**, 104052 (1999).

32. M. Shibata and K. Uryū, Phys. Rev. D **61**, 064001 (2000).

33. M. D. Duez, F. Foucart, L. E. Kidder, C. D. Ott, and S. A. Teukolsky, Class. Quantum Grav. **27**, 114106 (2010).

34. Y. Sekiguchi, K. Kiuchi, K. Kyotoku, and M. Shibata, Phys. Rev. Lett. **107**, 051102 (2011).

35. M. B. Deaton, M. D. Duez, F. Foucart, E. OConnor, C. D. Ott, L. E. Kidder, C. D. Muhlberger, M. A. Scheel, and B. Szilágyi, Astrophys. J. **776**, 47 (2013).

36. F. Foucart, M. B. Deaton, M. Duez, E. OConnor, C. D. Ott, R. Haas, L. E. Kidder, H. P. Pfeiffer, M. A. Scheel, and B. Szilagyi, Phys. Rev. D **90**, 024026 (2014).

37. C. Palenzuela, S.L. Liebling, D. Neilsen, L. Lehner, O.L. Caballero, E. O'Connor, and M. Anderson, Phys. Rev. D **92**, 044045 (2015).

38. Y. Sekiguchi, K. Kiuchi, K. Kyotoku, and M. Shibata, Phys. Rev. D **91**, 064059 (2015).

39. F. Foucart, E. O'Connor, L. Roberts, L. E. Kidder, J. Lippuner, H. P. Pfeiffer, and M. A. Scheel, Phys. Rev. D **94**, 123016 (2016).

40. K. Kiuchi, K. Kyotoku, Y. Sekiguchi, M. Shibata, and T. Wada, Phys. Rev. D **90**, 041502 (2014).

41. K. Kiuchi, P. Cerda-Duran, K. Kyotoku, Y. Sekiguchi, and M. Shibata, Phys. Rev. D **92**, 124034 (2015).

42. K. Kiuchi, Y. Sekiguchi, K. Kyotoku, M. Shibata, K. Taniguchi, and T. Wada, Phys. Rev. D **92**, 064034 (2015).

43. K. Hotokezaka, K. Kiuchi, K. Kyotoku, H. Okawa, Y. -i. Sekiguchi, M. Shibata and K. Taniguchi,Phys. Rev. D **87**, 024001 (2013).

44. F. Foucart, M. B. Deaton, M. D. Duez, L. E. Kidder, I. MacDonald, C. D. Ott, H. P. Pfeiffer, M. A. Scheel, B. Szilágyi, and S. A. Teukolsky, Phys. Rev. D **87**, 084006 (2013).

45. A. Bauswein, S. Goriely, H.-T. Janka, Astrophys. J. **773**, 78 (2013).

46. G. Lovelace, M. D. Duez, F. Foucart, L. E. Kidder, H. P. Pfeiffer, M. A. Scheel, and B. Szilágyi, Class. Quantum Grav. **30**, 135004 (2013).

47. K. Kyotoku, K. Ioka, and M. Shibata, Phys. Rev. D **88**, 041503(R) (2013).

48. F. Foucart, E. O'Connor, L. Roberts, M. Duez, R. Haas, L. E. Kidder, C. D. Ott, H. P. Pfeiffer, M. A. Scheel, and B. Szilagyi, Phys. Rev. D **91**, 124021 (2015).

49. F. Foucart, R. Haas, M. D. Duez, E. O'Connor, C. D. Ott, L. Roberts, L. E. Kidder, J. Lippuner, H. P. Pfeiffer, and M. A. Scheel, Phys. Rev. D **93**, 044019 (2016).

50. Y. Sekiguchi, K. Kiuchi, K. Kyotoku, M. Shibata, and K. Taniguchi, Phys. Rev. D **93**, 124046 (2016).

51. L. Lehner, S. L. Liebling, C. Palenzuela, O. L. Caballero, E. O'Connor, M. Anderson, and D. Neilsen, Class. Quantum Grav. **33**, 184002 (2016).

52. D. Radice, F. Galeazzi, J. Lippuner, L. F. Roberts, C. D. Ott, and L. Rezzolla, Mon. Not. R. Soc. Astron. **460**, 3255 (2016).

53. F. Foucart, D. Desai, W. Brege, M. D. Duez, D. Kasen, D. A. Hemberger, L. E. Kidder, H. P. Pfeiffer, and M. A. Scheel, Class. Quantum Grav. **34**, 044002 (2017).

54. K. Kyotoku, K. Kiuchi, Y. Sekiguchi, M. Shibata, and K. Taniguchi, Phys. Rev. D **97**, 023009 (2018).

55. T. Dietrich, M. Ujevic, W. Tichy, S. Bernuzzi, and B. Brügmann, Phys. Rev. D **95**, 024029 (2017).

56. T. Dietrich, S. Bernuzzi, M. Ujevic, and W. Tichy, Phys. Rev. D **95**, 044045 (2017).

57. L. Bovard, D. Martin, F. Guercilena, A. Arcones, and L. Rezzolla, and O. Korobkin, Phys. Rev. D **96**, 124005 (2017).

58. D. Radice, A. Perego, K. Hotokezaka, S. A. Fromm, S. Bernuzzi, and L. Roberts, Astrophys. J. **869**, 130 (2018).

59. S. Wanajo, Y. Sekiguchi, N. Nishimura, K. Kiuchi, K. Kyotoku, and M. Shibata, Astrophys. J. Lett. **789**, L39 (2014).

60. R. Fernández, F. Foucart, D. Kasen, J. Lippuner, D. Desai, and L. F. Roberts, Class. Quantum Grav. **34**, 154001 (2017).

61. R. Fernández and B. D. Metzger, Mon. Not. Royal Astron. Soc. **435**, 502 (2013).

62. B. D. Metzger and R. Fernández, Mon. Not. Royal Astron. Soc. **441**, 3444 (2014).

63. A. Perego, S. Rosswog, R. Cabezon, O. Korobkin, R. Kaeppeli, A. Arcones, M. Liebendoerfer, Mon. Not. Royal Astron. Soc. **443**, 3134 (2014).

64. R. Fernández, D. Kasen, B. D. Metzger, and E. Quataert, Mon. Not. Royal Astron. Soc. **446**, 750 (2015).

65. O. Just, A. Bauswein, R. A. Pulpillo, S. Goriely, and H.-Th. Janka, Mon. Not. Royal Astron. Soc. **448**, 541 (2015).

66. D. M. Siegel and B. D. Metzger, Phys. Rev. Lett. **119**, 231102 (2017).

67. S. Fujibayashi, K. Kiuchi, N. Nishimura, Y. Sekiguchi, and M. Shibata, Astrophys. J **860**, 64 (2018).

68. R. Fernández, A. Tchekhovskoy, E. Quataert, F. Foucart, D. Kasen, Mon. Not. R. Astron. Soc. **482**, 3373 (2019).

69. T.W. Baumgrate, S.L. Shapiro, and M. Shibata, Astrophys. J. Lett. **528**, L28 (2000).

70. M. Shibata, *Numerical Relativity* (World Scientific, 2016).

71. P. B. Demorest, T. Pennucci, S. M. Ransom, M. S. E. Roberts, and J. W. T. Hessels, Nature **467**, 1081 (2010).

72. J. Antoniadis et al., Science, **340**, 448 (2013).

73. M. Shibata, K. Taniguchi, and K. Uryū, Phys. Rev. D **71**, 084021 (2005).

74. M. Shibata and K. Taniguchi, Phys. Rev D **73**, 064027 (2006).

75. K. Kiuchi, Y. Sekiguchi, M. Shibata, and K. Taniguchi, Phys. Rev. D **80**, 064037 (2009).

76. K. Hotokezaka, K. Kyutoku, H. Okawa, M. Shibata, and K. Kiuchi, Phys. Rev. D **83**, 124008 (2011).

77. K. Hotokezaka, K. Kiuchi, K. Kyutoku, T. Muranushi, Y. -i. Sekiguchi, M. Shibata and K. Taniguchi,Phys. Rev. D **88**, 044026 (2013).

78. K. Takami, L. Rezzolla, and L. Baiotti, Phys. Rev. D **91**, 064001 (2015).

79. T. Dietrich, S. Bernuzzi, M. Ujevic, and B. Brügmann, Phys. Rev. D **91**, 124041 (2015).

80. S. Bernuzzi, D. Radice, C. D. Ott, L. F. Roberts, P. Moesta, and F. Galeazzi, Phys. Rev. D **94**, 024023 (2016).

81. R. Ciolfi, W. Kastaun, B. Giacomazzo, A. Endrizzi, D. M Siegel, and R. Perna, Phys. Rev. F **95**, 063016 (2017).

82. T. M. Tauris, et al., Astrophys. J. **846**, 170 (2017).

83. N. Pol, M. McLaughlin, and D. R. Lorimer, arXiv:1811.04086.

84. S. A. Balbus and J. F. Hawley, Rev. Mod. Phys. **70**, 1 (1998).

85. P. Meszaros and M. J. Rees, Astrophys. J. **397**, 570 (1992).

86. M. Ruffert and H.-Th. Janka, Astron. Astrophys. **344**, 573 (1996).

87. T. Di Matteo, R. Perna, and R. Narayan, Astrophys. J. **579**, 706 (2002).

88. W. H. Lee, E. Ramirez-Ruiz and D. Page, Astrophys. J. **632**, 421 (2005).

89. S. Setiawan, M. Ruffert and H.-Th. Janka, Mon. Not. R. Astron. Soc. **352**, 753 (2004).

90. M. Shibata, Y. Sekiguchi, and R. Takahashi, Prog. Theor. Phys. **118**, 257 (2007).

91. W.-X. Chen and A. M. Beloborodov, Astrophys. J. **657**, 383 (2007).

92. R. D. Blandford and R. L. Znajek, Mon. Not. R. Astron. Soc. **179**, 433 (1977).

93. J. C. McKinney, Mon. Not. R. Astron. Soc. **368**, 1561 (2006).

94. V. Paschalidis, M. Ruiz, and S. L. Shapiro, Astrophys. J. **806**, L14 (2015).

95. M. Ruiz, R. N. Lang, V. Paschlidis, and S. L. Shapiro, Astrophys. J. **824**, L6 (2016).

96. M. D. Duez, Y.-T. Liu, S. L. Shapiro, and B. C. Stephens, Phys. Rev. D **69**, 104030 (2004).

97. M. Shibata, K. Kiuchi, and Y. Sekiguchi, Phys. Rev. D **95**, 083005 (2017).

98. D. J. Price and S. Rosswog, Science **312**, 719 (2006).

99. K. Kiuchi, K. Kawaguchi, K. Kyutoku, Y. Sekiguchi, and M. Shibata, Phys. Rev. D **97**, 124039 (2018).

100. S. Chandrasekhar, *Hydrodynamic and Hydromagnetic Stability* (Oxford University Press, 1961)

101. N. I. Shakura and R. A. Sunyaev, Astron. Astrophys. **24**, 337 (1973).

102. J. F. Hawley, S. A. Richers, X. Guan, and J. H. Krolik, Astrophys. J. **772**, 102 (2013).

103. T. K. Suzuki and S. Inutsuka, Astrophys. J. **784**, 121 (2014).

104. J. M. Shi, J. M. Stone, and C. X. Huang, Mon. Not. R. Soc. Astron. **456**, 2273 (2016).

105. J. L. Friedman, J. R. Ipser, and L. Parker, Astrophys. J. **304**, 115 (1986).

106. G.B. Cook, S.L. Shapiro, and S.A Teukolsky, Astrophys. J. **423**, 823 (1994).

107. M. Shibata and K. Uryū, Phys. Rev. D **74**, 121503(R) (2006).

108. K. Kyutoku, M. Shibata, and K. Taniguchi, Phys. Rev. D **82**, 044049 (2010).

109. K. Kyutoku, H. Okawa, M. Shibata, and K. Taniguchi, Phys. Rev. D **84**, 064018 (2011).

110. F. Foucart, M. D. Duez, L. E. Kidder, and S. A. Teukolsky, Phys. Rev. D **83**, 024005 (2012).

111. F. Foucart, M. D. Duez, L. E. Kidder, M. A. Scheel, B. Szilágyi, and S. A. Teukolsky, Phys. Rev. D **85**, 044015 (2012).

112. K. Kawaguchi, K. Kyutoku, H. Nakano, H. Okawa, M. Shibata, and K. Taniguchi, Phys. Rev. D **92**, 024014 (2015).

113. K. Kyutoku, K. Ioka, H. Okawa, M. Shibata, and K. Taniguchi, Phys. Rev. D **92**, 044028 (2015).

114. K. Hotokezaka, K. Kiuchi, M. Shibata, E. Nakar, and T. Piran, Astrophys. J. **867**, 95 (2018).

115. J. Lippuner and L. F. Roberts, Astrophys. J. **815**, 82 (2015).

116. D. Kasen, R. Fernández, B. D. Metzger, Mon. Not. R. Astro. Soc. **450**, 1777 (2015).

117. J. Lippuner, R. Fernández, L. Robert, F. Foucart, D. Kasen, B. D. Metzger, and C. D. Ott, Mon. Not. R. Soc. Astron. **472**, 904 (2017).

118. Y.-Z. Qian and S. E. Woosley, Astrophys. J. **471**, 331 (1996).

119. K. Hotokezaka, R. Sari, and T. Piran, Mon. Not. Roy. Astron. Soc. **468**, 91 (2017).

120. M.-R. Wu, J. Barnes, G. Martinez-Pinedo, B. D. Metzger arXiv:1808.10459

121. K. Hotokezaka, S. Wanajo, M. Tanaka, A. Bamba, Y. Terada, and T. Piran, Mon. Not. R. Astron. Soc. **459**, 35 (2016).

122. Y. Zhu, et al., Astrophys. J. Lett. **863**, L23 (2018).

123. J. Barnes, D. Kasen, M.-R. Wu, G. Martinez-Pinedo, Astrophys. J. **829**, 110 (2016).

124. D. Kasen and J. Barnes, arXiv:1807.03319

125. D. Kasen, N. R. Badnell, and J. Barnes, Astrophys. J. **774**, 25 (2013).

126. M. Tanaka et al., Astrophys. J. **852**, 109 (2018).

127. R. T. Wollaeger et al., Mon. Not. Roy. Soc. **478**, 3298 (2018).

128. K. Hotokezaka1, S. Nissanke, G. Hallinan, T. J. W. Lazio, E. Nakar, and T. Piran, Astrophys. J. **831**, 190 (2016).

129. E. Waxman, E. Ofek, D. Kushnir, and A. Gal-Yam, Mon. Not. Roy. Soc. **481**, 3423 (2018).

130. I. Arcavi Astrophys. J. **855**, L23 (2018).

131. M. M. Kasliwal, et al., Mon. Not. Roy. Soc., L41 (2019).

132. D. Kasen, B. D. Metzger, J. Barnes, E. Quataert and E. Ramirez-Ruiz, Nature **551**, 7678 (2017).

133. A. A. Villar et al., Astrophys. J. Lett. **851**, L21 (2017).

134. E. Nakar, O. Gottlieb, T. Piran, M. M. Kasliwal and G. Hallinan, Astrophys. J. **867**, 18 (2018).

135. A. Perego, D. Radice, and S. Bernuzzi, Astrophys. J. Lett. **850**, L37 (2017).

136. M. Shibata, S. Fujibayashi, K. Hotokezaka, K. Kiuchi, K. Kyutoku, Y. Sekiguchi and M. Tanaka, Phys. Rev. D **96**, 123012 (2017).

137. K. Kawaguchi, M. Shibata, and M. Tanaka, Astrophys. J. Lett. **865**, L21 (2018).

138. E. Troja, et al., Nature **551**, 71 (2017).
139. G. Hallinan, et al., Science **358**, 6370 (2017).
140. K. P. Mooley, et al., Nature **554**, 7691 (2018).
141. E. Troja, et al., Mon. Not. Roy. Astron. **487**, L18 (2018).
142. K. P. Mooley, et al., Astrophys. J. Lett. **868**, L21 (2018).
143. R. Margutti, et al., Astrophys. J. Lett. **856**, L18 (2018).
144. K. P. Mooley, et al., Nature **561**, 7723 (2018).
145. B. P. Abbott et al., Astrophys. J. Lett. **848**, L13 (2017).
146. O. Gottlieb, E. Nakar, T. Piran, and K. Hotokezaka, Mon. Not. Roy. Soc. **479**, 588 (2018).
147. M. Ruiz and S. L. Shapiro, Phys. Rev. D **96**, 084063 (2017).
148. H. Nagakura, K. Hotokezaka, Y. Sekiguchi and M. Shibata, Astrophys. J. Lett. **784**, L28 (2014).
149. A. Murguia-Berthier, G. Montes, E. Ramirez-Ruiz, F. De Colle and W. H. Lee, Astrophys. J. Lett. **788**, L8 (2014).
150. P. C. Duffell, E. Quataert, and A. I. MacFadyen, Astrophys. J. **813**, 64 (2015).